Pergamon

Formation of refractory inclusions by evaporation of condensate precursors

LAWRENCE GROSSMAN,*,† DENTON S. EBEL,‡ and STEVEN B. SIMON

Department of the Geophysical Sciences, The University of Chicago, 5734 South Ellis Ave., Chicago, IL 60637, USA

Abstract—Berman's (1983) activity-composition model for $CaO-MgO-Al_2O_3-SiO_2$ liquids is used to calculate the change in bulk chemical and isotopic composition during simultaneous cooling, evaporation, and crystallization of droplets having the compositions of reasonable condensate precursors of Types A and B refractory inclusions in CV3 chondrites. The degree of evaporation of MgO and SiO_2, calculated to be faithfully recorded in chemical and isotopic zoning of individual melilite crystals, is directly proportional to evaporation rate, which is a sensitive function of P_{H_2}, and inversely proportional to the droplet radius and cooling rate. When the precursors are partially melted in pure hydrogen at peak temperatures in the vicinity of the initial crystallization temperature of melilite, their bulk chemical compositions evolve into the composition fields of refractory inclusions, mass-fractionated isotopic compositions of Mg, Si, and O are produced that are in the range of the isotopic compositions of natural inclusions, and melilite zoning profiles result that are similar to those observed in real inclusions. For droplets of radius 0.25 cm evaporating at $P_{H_2} = 10^{-6}$ bar, precursors containing 8 to 13 wt.% MgO and 20 to 23% SiO_2 evolve into objects similar to compact Type A inclusions at cooling rates of 2 to 12 K/h, depending on the precise starting composition. Precursors containing 13 to 14 wt.% MgO and 23 to 26% SiO_2 evolve into objects with the characteristics of Type B1 inclusions at cooling rates of 1.5 to 3 K/h. The relatively SiO_2-poor members of the Type B2 group can be produced from precursors containing 14 to 16 wt.% MgO and 27 to 33% SiO_2 at cooling rates of <1 K/h. Type B2's containing 27 to 35 wt.% SiO_2 and <12% MgO require precursors with higher SiO_2/MgO ratios at MgO > 15% than are found on any condensation curve. The characteristics of fluffy Type A inclusions, including their reversely zoned melilite, can only be understood in the context of this model if they contain relict melilite. *Copyright © 2002 Elsevier Science Ltd*

1. INTRODUCTION

The bulk chemical compositions of most Types A and B, Ca-, and Al-rich, refractory inclusions in Allende and other CV3 chondrites are depleted in MgO and SiO_2 relative to CaO and Al_2O_3, compared to compositions of calculated equilibrium assemblages of condensates from solar and dust-enriched gases (Grossman et al., 2000). Many of these objects existed as melt droplets from which a fassaitic pyroxene crystallized whose Ti^{3+}/Ti^{4+} ratio indicates that the melt solidified under an oxygen fugacity equal to that of a hydrogen-rich gas of solar composition (Beckett, 1986). Davis et al. (1998) showed experimentally that MgO and SiO_2 preferentially evaporate from droplets having compositions similar to those of Type B inclusions when the droplets are immersed in hydrogen-rich gas at 1500°C. Grossman et al. (2000) developed a thermodynamic model for calculating the equilibrium vapor pressure of a nonideal, $CaO-MgO-Al_2O_3-SiO_2$ (CMAS) liquid in vacuum and pure H_2. They used it to show that removal of the relative amounts of MgO and SiO_2 predicted to evaporate at 1700 K from melt droplets having the bulk chemical compositions of high-temperature condensate assemblages would yield residues having the bulk compositions of Types A and B inclusions. Grossman et al. (2000) further showed that the absolute amounts required to be evaporated are consistent with available

data on the degree of Mg and Si isotopic mass-fractionation in bulk inclusions.

It is unlikely, however, that these inclusions were either at constant temperature or in the totally molten state when they underwent evaporation. In a study of the liquid-crystal phase relations of a Type A–like composition, #98, Paque and Stolper (1984) found that spinel crystallizes on the liquidus at 1810 K and melilite begins to form at 1783 K. On the basis of melilite textures, they concluded that the maximum temperature reached by inclusions of this composition was below the liquidus. Relict melilite grains are rare in compact Type A's (Simon et al., 1999), suggesting these inclusions experienced peak temperatures close to that for initial crystallization of melilite. According to Stolper (1982), the sequence of minerals that form during cooling and equilibrium crystallization of a liquid of Type B–like composition, CAIB, is spinel, melilite, anorthite, and fassaitic clinopyroxene. The liquidus temperature for this composition was estimated at 1823 K. Stolper and Paque (1986) reasoned, primarily from the textures and compositions of melilite crystals in Type B inclusions, that the maximum temperature reached before cooling was within 20 K of the temperature at which melilite begins to crystallize, which is 1675 K for CAIB. The solidus temperature for all Types A and B inclusion compositions is near 1500 K. It is thus likely that the evaporation process that left its imprint on the chemical and isotopic compositions of refractory inclusions occurred during cooling and crystallization from ~1800 K for Type A's and ~1700 K for Type B's to 1500 K.

Grossman et al. (2000) found that the ratio of the vapor pressure of $Mg_{(g)}$ to that of $SiO_{(g)}$ over CMAS liquids is

* Author to whom correspondence should be addressed (yosi@midway.uchicago.edu).
† Also Enrico Fermi Institute, The University of Chicago.
‡ *Present address:* Department of Earth and Planetary Sciences, American Museum of Natural History, New York, NY 10024.

Table 1. Compositions (wt.%) of high-temperature condensate assemblages used as starting compositions for evaporation computations in this work, calculated on a metal- and TiO_2-free basis.

Composition	CaO	MgO	Al_2O_3	SiO_2
α	31.78	8.30	40.17	19.74
β	28.56	12.56	36.08	22.79
χ	26.59	13.80	33.60	26.00
δ	24.37	15.07	30.79	29.77
ϕ	22.58	16.15	28.53	32.74

sensitive to both temperature and liquid composition. Furthermore, the evaporation coefficients that relate the pressures of these species to their respective loss rates decline with falling temperature (Richter et al., in press). Because the actual temperature range over which evaporation occurred was different from that modeled by Grossman et al. (2000), and because the liquid compositions were changing due to precipitation of solid phases in addition to evaporation, it is far from clear that the agreement between the degree of evaporation calculated from their model and that obtained from the isotopic compositions of inclusions would persist in a more realistic model. Thus, the purpose of this paper is to model the chemical and isotopic evolution, during cooling and crystallization, of droplets with initial bulk chemical compositions of high-temperature condensates; to explore the effects of P_{H_2}, droplet size, and cooling rate on their final bulk chemical and isotopic compositions as well as on the zonation of these properties within melilite grains that crystallize from them; and, by comparison of these predicted properties with those of actual inclusions, to constrain the physicochemical conditions under which refractory inclusions evolved.

2. TECHNIQUE

2.1. Input Assumptions

2.1.1. Initial Chemical Compositions

During condensation, the bulk chemical composition of the condensed fraction of solar system matter changes continuously with falling temperature, as more and more material condenses into it. As in Grossman et al. (2000), any composition lying along the trajectory of bulk chemical compositions of high-temperature condensate assemblages predicted to form in a solar gas between 1350 and 1310 K at $P^{tot} = 10^{-5}$ bar is considered a possible precursor composition for Types A and B inclusions. The specific bulk chemical compositions investigated in this work, α, β, χ, δ, and ϕ, are calculated on a TiO_2- and metallic iron–free basis, and given in Table 1.

2.1.2. Thermodynamic Data for Silicate Liquids

A model for the thermodynamic properties of silicate liquids having the compositions of refractory inclusions is needed to calculate both their liquid-crystal equilibrium assemblages and their vapor pressures. In this work, as in Grossman et al. (2000), the 1.0 to 1.5 wt.% TiO_2 present in refractory inclusions is ignored, and Berman's (1983) activity-composition relations for CMAS liquids are used. For vapor pressure cal-

culations, the same gas species and sources of their thermodynamic data are used as in Grossman et al. (2000).

2.1.3. Thermodynamic Data for Minerals

Experimental liquid-crystal phase relations on CAIB (Stolper, 1982) show that the evolution of the liquid is controlled by crystallization of spinel and melilite, as anorthite and clinopyroxene crystallize very late, almost on the solidus. In this work, therefore, crystallization of the latter two phases is ignored. This is equivalent to assuming that they both crystallize from whatever liquid remains at 1500 K. Thermodynamic data for $MgAl_2O_4$ spinel are taken from Berman (1988).

In this work, melilite is treated as a nonideal solid solution of the two end-members, gehlenite ($Ca_2Al_2SiO_7$) and åkermanite ($Ca_2MgSi_2O_7$). An attempt was made to use Berman's (1983) end-member data together with the nonideal, gehlenite-åkermanite mixing model of Charlu et al. (1981) and Berman's (1983) liquid model to calculate the temperatures of first crystallization of melilite and of disappearance of liquid for a number of different bulk compositions along the gehlenite-åkermanite binary, i.e., the liquidus and solidus, respectively. Results are shown in Figure 1, where they are compared with the liquidus and solidus curves obtained experimentally by Osborn and Schairer (1941). It is seen that this model is very unsatisfactory in that it predicts a liquidus loop that is too narrow, and liquidus and solidus temperatures that are too high, compared to the experimental melting relations, with the difference between predicted and measured liquidus curves increasing with increasing åkermanite content and reaching over 100 K by $Åk_{60}$. Two other sets of calculated curves are shown in Figure 1. For calculating equilibrium between melilite and their MELTS liquid model, Ghiorso and Sack (1995) combined Berman's (1988) end-member thermodynamic data for melilite with Charlu et al.'s (1981) mixing model. When the above calculation is repeated using this combination of melilite data with Berman's (1983) liquid model, it is seen in Figure 1 that the melting points of pure gehlenite and pure åkermanite are now underestimated by 90 and 130 K, respectively. In this calculation, however, the liquidus loop is wider, and although the difference between the observed and predicted liquidus temperatures increases with decreasing åkermanite content and reaches 70 K at $Åk_{20}$, predicted solidus temperatures are within 20 K of the measured ones in the range $Åk_{20}$ to $Åk_{60}$. The final pair of curves is obtained when the thermodynamic data for gehlenite from Berman (1983) and those for åkermanite from Berman (1988) are combined with an asymmetric regular solution formulation of the mixing properties of melilite solid solutions in which the two Margules parameters are adjusted arbitrarily to obtain the best fit between predicted and observed liquidus loops. It is seen that very good agreement is achieved for all compositions between $Åk_0$ and $Åk_{\sim45}$, where the compositions of most melilite grains in Types A and B inclusions lie. Note that none of the models investigated here is capable of reproducing the smaller loop at $Åk_{>72}$, the composition with the minimum melting temperature.

The accuracy of the latter two models was tested further by using each of them with Berman's (1983) liquid model to calculate the evolution of solid and liquid compositions during equilibrium crystallization of spinel and melilite from four
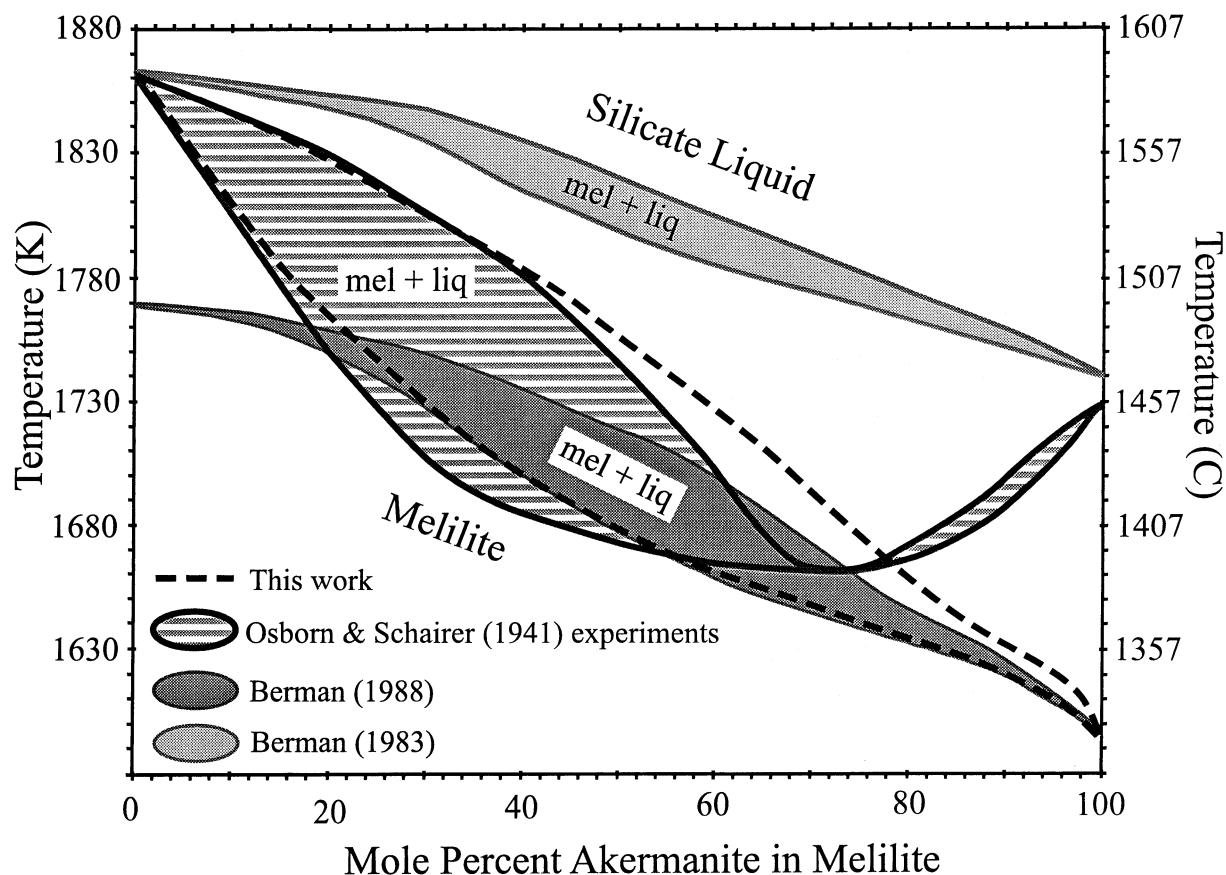
Fig. 1. Experimentally determined, liquid-crystal phase relations in the gehlenite-åkermanite binary compared to liquidus loops calculated with Berman's (1983) $CaO-MgO-Al_2O_3-SiO_2$ liquid model using several different thermodynamic models for melilite. One uses melilite end-member data from Berman (1983), another from Berman (1988). The one used in this work combines Berman's (1983) data for gehlenite with Berman's (1988) data for åkermanite.

inclusion-like bulk compositions whose liquid-crystal phase relations have been experimentally investigated. In Table 2, the temperature and åkermanite content of the first melilite observed to crystallize upon cooling are compared to those predicted using the old and new melilite models, i.e., Berman's (1988) end-member data with Charlu et al.'s (1981) mixing model, and the asymmetric regular solution model, respectively. Use of the new model increases the predicted appearance temperatures of melilite by 30 to 50 K and decreases the predicted Åk content of the first melilite by 7 to 13 mol.%

compared to the old model. These changes are seen to produce substantially better agreement between observations and predictions, except in the cases of melilite appearance temperatures for the Type B1-1 and CAIB compositions. In Figure 2, the curve of evolution of liquid compositions, called the liquid line of descent, observed upon cooling and crystallization of three of these bulk compositions, is also compared to that predicted using each of the old and new melilite models. The new melilite model is seen to yield liquid compositions for FTA and CTA that are much closer to the experimental data

Table 2. Compositions and temperatures of appearance of the first melilite to crystallize upon cooling from four different synthetic liquid compositions. Experimental data are compared to predictions using two different melilite solution models, old and new (see text).

| Synthetic sample | Bulk composition (wt.%) | | | | | First melilite to crystallize | | | | | |
| | | | | | | Appearance temperature (K) | | | mol. % åkermanite | | |
	CaO	MgO	Al_2O_3	SiO_2	TiO_2	Obs	Old	New	Obs	Old	New
FTA	34.61	5.23	37.36	21.53	1.21	1801	1748	1802	1.4	12.8	5.5
CTA	35.52	6.28	31.71	25.12	0.48	1793	1742	1796	1.8	18.5	8.9
B1-1	28.11	8.49	31.68	27.59	4.07	1705	1680	1734	15.8	24.7	13.5
CAIB	29.2	10.1	28.3	31.1	1.12	1673	1680	1708	22.0	31.2	18.6

All experimental data (Obs) are from Beckett (1986) except those for CAIB, which are from Stolper (1982).

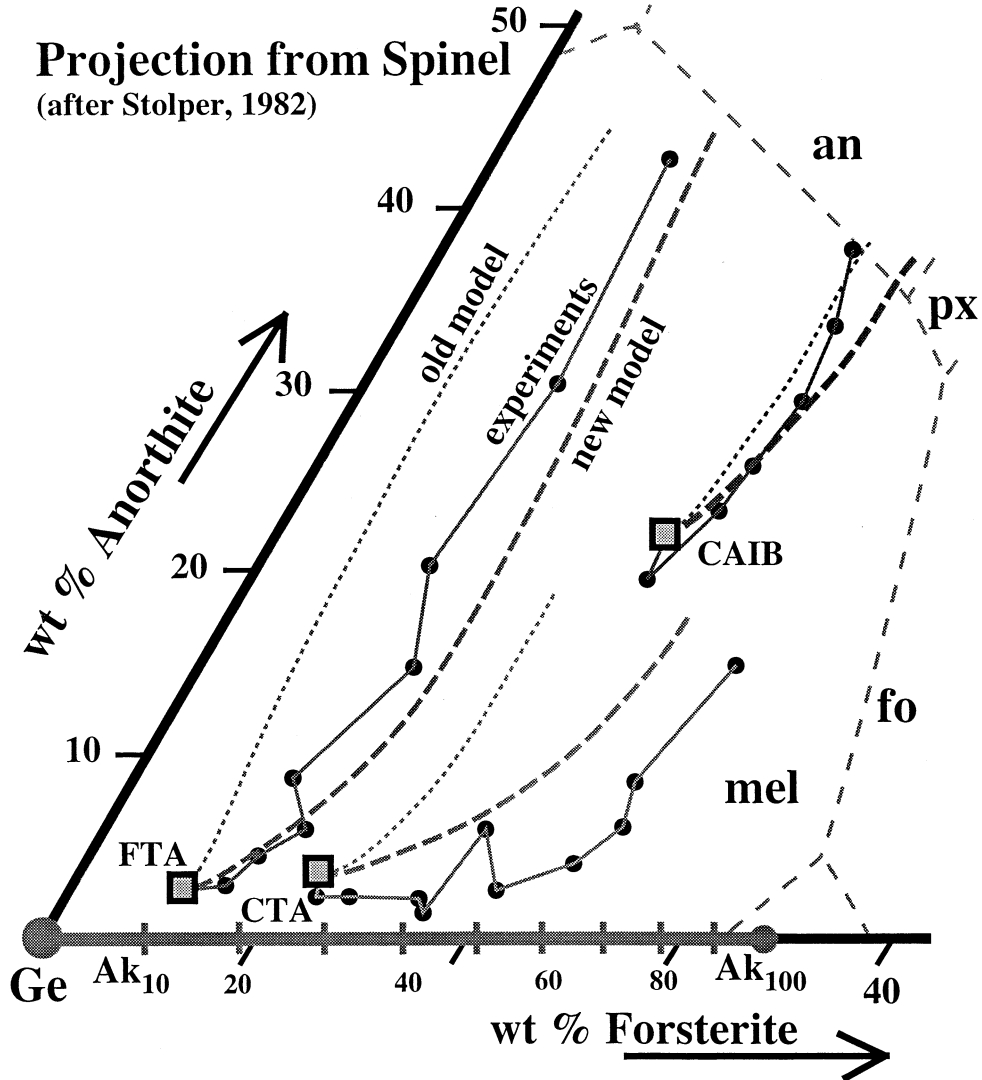**Projection from Spinel**
(after Stolper, 1982)

Fig. 2. Comparison of predicted vs. experimentally determined (solid lines connecting points) paths of liquid composition due to crystallization of spinel and melilite with falling temperature, from each of three synthetic starting compositions, all projected from spinel onto the gehlenite-rich corner of the anorthite-gehlenite-forsterite plane. Old model (short dashes) refers to calculations using Berman's (1988) end-member data for melilite, and new model (long dashes) to the model used in this work. Composition fields where spinel coexists with each of melilite, anorthite, clinopyroxene, and forsterite are labeled mel, an, px, and fo, respectively. Positions of various melilite solid solution compositions are indicated along the gehlenite-forsterite axis.

than the old model, but for CAIB, the new melilite model gives a better fit to the higher temperature liquid compositions and the old model is better for the lower temperature ones.

2.1.4. Calculation of Evaporation Effects

The partial pressures of all gas species in equilibrium with all liquid compositions considered in this work are calculated in exactly the same way as in Grossman et al. (2000). As in that work, P_{Mg} and P_{SiO} increase with increasing activity of MgO and SiO$_2$, respectively, in the liquid and with increasing P_{H_2} in the surrounding gas, and are always much higher than the partial pressures of all other species. Because of this, the change in composition of a CMAS liquid during evaporation

depends primarily on the fluxes of Mg$_{(g)}$ and SiO$_{(g)}$. When the concentrations of these species in the ambient gas are zero, their free evaporation fluxes from a liquid droplet can be obtained from their equilibrium partial pressures via the Hertz-Knudsen equation:

$$J_{SiO} = \alpha_{SiO} \, P_{SiO}/(2\pi m_{SiO}kT)^{0.5}, \qquad (1)$$

and

$$J_{Mg} = \alpha_{Mg} \, P_{Mg}/(2\pi m_{Mg}kT)^{0.5}, \qquad (2)$$

where k is the Boltzmann constant, T is the absolute temperature, and J, α, and m are the flux, evaporation coefficient, and atomic mass of each evaporating species, respectively. In using

these expressions, zero back-condensation of evaporating species is assumed, such as would be the case for a small droplet in an infinite reservoir.

Richter et al. (in press) conducted evaporation experiments on a droplet of initial composition 22.64 wt.% CaO, 11.94% MgO, 19.30% Al_2O_3, and 46.04% SiO_2 at 2073 K in a vacuum, and separately on a droplet of initial composition 24.61 wt.% CaO, 17.84% MgO, 20.51% Al_2O_3, and 37.04% SiO_2 at 1773 K and at a P_{H_2} of 1.87×10^{-4} bar. J_{SiO} and J_{Mg} were measured for each experiment and combined with P_{SiO} and P_{Mg} calculated for each experiment by the method of Grossman et al. (2000) to yield α_{SiO} and α_{Mg} using Eqn. 1 and 2. When the values obtained for α_{Mg} (0.17 ± 0.05 at 2073 K and 0.040 ± 0.011 at 1773 K) are plotted on a log α vs. $1/T$ graph, the straight line through them also lies along the trend obtained for α from forsterite evaporation experiments in a vacuum (Wang et al., 1999) and in H_2 (Kuroda and Hashimoto, 2000). Extrapolating the CMAS data along this line to the temperature range of interest suggests that α_{Mg} varies from 0.050 at 1813 K to 0.0065 at 1500 K. Richter et al. (in press) found that the bulk chemical compositions of the evaporation residues in the vacuum experiment were fit by an α_{SiO}/α_{Mg} ratio of 1.00, while Grossman et al. (2000) found that the best fit to the residues in the hydrogen experiment is obtained with an α_{SiO}/α_{Mg} ratio of 1.35. In this work, the latter value of the α_{SiO}/α_{Mg} ratio was used in combination with the temperature variation of α_{Mg} to obtain the variation of α_{SiO} with temperature.

Droplet radii were corrected for evaporative mass loss using a composition-independent liquid density of 3.1 g/cm³ based on data from Lange and Carmichael (1987), and for crystallization of spinel and melilite using densities of 3.58 and 3.0 g/cm³, respectively, from Robie et al. (1978). In the model, spinel and melilite crystals are assumed not to reside on the droplet surface where they would otherwise reduce the liquid surface area. All of the liquid is assumed to be instantaneously in chemical communication with a vapor phase consisting of pure H_2, and crystalline solids are assumed to undergo negligible evaporation on the time scale of crystallization of the droplets.

As in Grossman et al. (2000), the isotopic mass-fractionations of Mg and Si, F_{Mg} and F_{Si}, respectively, expressed in per mil per atomic mass unit are calculated from the computed amount of evaporative mass loss of each of these elements, using the Rayleigh equation in which the fractionation factors are the inverse square roots of the masses of the evaporating species, $Mg_{(g)}$ and $SiO_{(g)}$, respectively, at each temperature step. In the case of oxygen, the inverse square roots of the masses of the isotopic species of $SiO_{(g)}$ and $H_2O_{(g)}$ are weighted in proportion to the relative vapor pressures of these molecules at each temperature step to obtain the fractionation factor.

2.1.5. Equilibration of Phases

Estimates were made of the ability of spinel and melilite, separately, to exchange Mg with the liquid as it cooled and changed composition. The average spinel crystal in Allende refractory inclusions has a radius of ~14 μm. For cooling intervals representative of those investigated in this paper for precursors of Types A and B inclusions, 1800 to 1500 K and 1675 to 1500 K, respectively, average linear growth rates were

calculated for spinel as a function of cooling rate for each inclusion type simply by dividing the average radius by the cooling time. Similarly, from data for Mg self-diffusion in $MgAl_2O_4$ measured by Sheng et al. (1992), mean diffusion rates were calculated as a function of cooling rate by dividing the cooling time into the diffusion distance computed from the average diffusion coefficient for the temperature interval appropriate for each inclusion type. This calculation shows that the diffusion rate is faster than the growth rate for all cooling rates below ~30 K/h for Type A precursors, and below ~5 K/h for Type B precursors. It can therefore be assumed that spinel crystals grew in complete Mg isotopic equilibrium with the liquid for all but the very fastest cooling rates considered here for Type A's, and for cooling rates below 5 K/h for the Type B's.

The situation is different for melilite because its crystals are much larger than those of spinel, and the (Al + Al) − (Mg + Si) interdiffusion coefficient for melilite is ~10 to 50 times smaller than the self-diffusion coefficient for spinel in this temperature range, according to the data of Morioka and Nagasawa (1991). The average minimum and average maximum dimensions were measured for 10 melilite crystals in each of two compact Type A, three Type B1, and two Type B2 inclusions from Allende. Combining the smallest average minimum dimension found, 175 μm, with the same cooling intervals used for spinel, average linear growth rates were calculated for melilite as a function of cooling rate for each inclusion type in the same way as for spinel. Using interdiffusion coefficients for åkermanite contents and temperature intervals appropriate for each inclusion type, mean interdiffusion rates were calculated in the same way as for spinel, and were found to be 3 to 250 times slower than the melilite growth rates under these conditions. Only at very slow cooling rates, $<2 \times 10^{-2}$ K/h for Type A's and $<1 \times 10^{-3}$ K/h for Type B's, are the interdiffusion rates comparable to the growth rates. On this basis, it seems likely that progressive growth of melilite crystals effectively isolates their interiors from chemical communication with the coexisting liquid. This prevents chemical and isotopic exchange of Mg and Si, and equilibration of the composition of interior melilite, with the liquid from which the outermost melilite is precipitating at any instant for all cooling rates considered here.

In Types A and B inclusions, spinel crystals were poikilitically enclosed by melilite while the latter crystallized from the liquid. Even while the centers of those spinel crystals that remain in contact with the liquid can equilibrate with it, the very limited ability of Mg to diffuse into the interiors of the melilite crystals causes chemical isolation of those spinel grains trapped inside melilite. In the model, spinel grains are assumed to be homogeneously distributed throughout the liquid, so that the fraction of the spinel grains trapped inside melilite can be assumed to be equal to the volume fraction of the liquid converted to melilite at each temperature step.

Using lattice diffusion data for oxygen in melilite from Yurimoto et al. (1989), estimates were made of the oxygen diffusion coefficients parallel to the fastest diffusion direction, the a-axis, as a function of åkermanite content and temperature. These are on the order of 1 to 3×10^{-12} cm²/s for the melilite compositions and temperature ranges used here for Types A
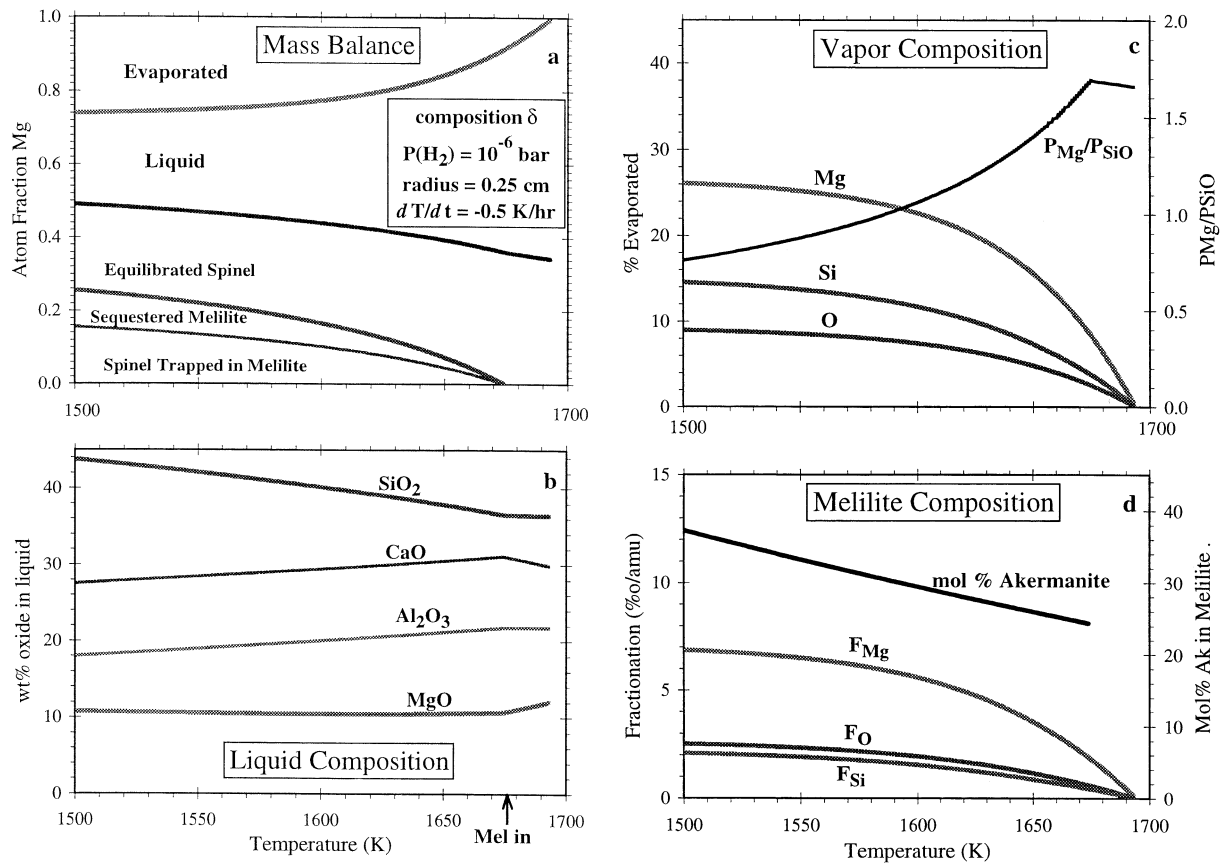
Fig. 3. Evolution of liquid, vapor, and melilite composition during simultaneous cooling, evaporation, and crystallization for the conditions indicated, plotted as a function of temperature. (a) Distribution of Mg between vapor, liquid, and solids. (b) Evolution of the bulk chemical composition of the liquid. (c) Cumulative fraction of the initial magnesium, silicon, and oxygen evaporated from the droplet, and instantaneous P_{Mg}/P_{SiO} ratio of the escaping vapor. (d) Magnesium, silicon, and oxygen isotopic composition of the liquid and thus of the melilite crystallizing at each temperature, along with its åkermanite content.

and B inclusions. As these values are quite comparable to the (Al + Al) − (Mg + Si) interdiffusion coefficients used above, it seems unlikely that melilite would undergo significant oxygen isotopic exchange with the liquid during cooling on the time scales considered here.

In spinel, the diffusion coefficient for oxygen is 4 or 5 orders of magnitude lower than for Mg at the same temperature (Ryerson and McKeegan, 1994). Thus, while it is concluded above that spinel probably maintains Mg isotopic equilibrium with the liquid for most of the thermal histories considered here, this will not be the case for oxygen. Nevertheless, throughout this paper, spinel is modeled as if it maintains isotopic equilibrium with the liquid for both magnesium and oxygen. The justification for this is that bulk oxygen isotopic compositions calculated in a run in which oxygen in spinel that remains in contact with the liquid equilibrates totally with that liquid (the "equilibration case") are little different from an otherwise identical run in which oxygen in all spinel is sequestered. The factors contributing to this outcome are common to all of our run results. Spinel normally contains only 15 to 20% of the entire oxygen budget of the system. The peak temperature is always slightly above the temperature at which melilite begins to crystallize. At such peak temperatures, 80 to 90% of

the spinel is already crystalline, as in Figure 3a. Because no evaporation is assumed to occur before reaching the peak temperature, this initial spinel isolates 12 to 18% of the total oxygen with normal isotopic composition in the sequestration case. Even in the equilibration case, however, two thirds of all spinel becomes encased in melilite, after which point it cannot equilibrate with the liquid anyway. In the equilibration case, then, the additional oxygen that equilibrates with the liquid, which cannot do so in the sequestration case, is only a little more than 5 to 7% of the total. As a result, the additional amount by which the bulk oxygen isotopic composition is mass-fractionated in the equilibration case relative to the fractionation case is less than 0.1‰. Toward the end of the cooling period, however, large amounts of oxygen have been isolated from evaporation by its sequestration into melilite and the spinel enclosed within it, and the effect of evaporation on the isotopic composition of the residual liquid is amplified, producing much larger mass-fractionations in the liquid than in the bulk assemblage. Because of this, even the small amount (5 to 7%) of additional oxygen that is in the spinel in equilibrium with the liquid represents a relatively large fraction of the evaporating pool, resulting in significantly less mass-fractionation in the final liquids in the equilibration case reported in this

paper than would be the case for the more realistic sequestration case.

2.2. The Model

For each computation, an initial bulk chemical composition is selected from Table 1. The initial Mg and Si isotopic compositions are assumed to be normal. For the molten droplet, a starting temperature slightly above that at which melilite is calculated to begin crystallizing from the assumed starting composition is selected, and an initial radius is specified. A cooling rate and P_{H_2} are specified for the surrounding gas. A time step size is selected that is appropriate for the assumed cooling rate, usually resulting in temperature differences of 0.5 to 1.5 K between steps. At each temperature, the equilibrium amounts of spinel, melilite, and liquid are calculated, as well as the chemical compositions of melilite and liquid. The Mg, Si, and O isotopic compositions of the melilite and spinel that form at each temperature are assumed to be the same as those of the coexisting liquid. The amount of spinel enclosed by melilite is computed, and its isotopic composition remains constant for the duration of the calculation. The droplet radius is corrected for the volume change due to the calculated amount of liquid converted to crystals. Next, the composition of the vapor in equilibrium with the calculated liquid composition is computed and, from P_{Mg} and P_{SiO}, the evaporative fluxes of $Mg_{(g)}$ and $SiO_{(g)}$ are obtained. The surface area of the droplet is calculated, and the fluxes are then used to calculate the amounts of MgO and SiO_2 lost from the droplet during the time step taken to cool to the next temperature. These evaporative mass losses are used to recalculate the Mg and Si isotopic compositions of the liquid and the radius of the droplet. Together with the amount of sequestered melilite and of the spinel within it, the evaporative mass losses are subtracted from the starting bulk composition to calculate the bulk chemical composition of the system that can undergo liquid-crystal equilibration at the next temperature. Then the entire computation is repeated, starting with the equilibrium amounts of spinel, melilite, and liquid present in the modified bulk chemical composition at the lower temperature. The chemical and isotopic composition of the spinel not enclosed by melilite at the previous temperature is included in computing the composition of the liquid from which fresh spinel and melilite crystallize. This process is continued until the solidus temperature is reached.

3. RESULTS

3.1. Melilite Zoning

The experimentally determined liquid-crystal phase relations along the gehlenite-åkermanite binary (Fig. 1) show that both liquidus and solidus temperatures gradually decline with increasing åkermanite content for all melilite from $Åk_0$ to $Åk_{73}$, the composition with the minimum melting temperature. With only a very few exceptions, all melilite in refractory inclusions lies within this range. This means that, for a given bulk composition, the first melilite to form during equilibrium cooling and crystallization in a closed system has the lowest åkermanite content, that its formation enriches the liquid in MgO and SiO_2 relative to Al_2O_3 compared to the starting composition, and that melilite that crystallizes at progressively lower temperatures

has progressively higher Åk contents. Phase equilibrium experiments in the CMAS system show that melilite cocrystallizing with spinel also continuously increases its åkermanite content with falling temperature (Stolper, 1982; Beckett, 1986). To maintain equilibrium as the temperature falls, early formed, relatively åkermanite-poor melilite must continuously increase its åkermanite content by diffusion driven exchange of its Al^{3+} ions with Mg^{2+} and Si^{4+} in the liquid. Failure of the diffusion rate to keep pace with the crystallization rate results in normally zoned crystals whose åkermanite contents increase from their cores toward their outer rims.

In an open system in which evaporation of MgO and SiO_2 takes place while the temperature is falling, the resulting decrease with time in the MgO and SiO_2 contents of the liquid counteracts the thermodynamic tendency of melilite crystals to increase their åkermanite contents with falling temperature. In this situation, if the evaporation time is short compared to the cooling time, the first melilite to crystallize may be the most åkermanitic, and reversely zoned crystals, in which the åkermanite content steadily decreases from their cores to their rims, may result.

The evaporation time, τ, in hours, of a volatile element is given by the amount initially present, divided by its loss rate, as in

$$\tau = \frac{4/3 \pi a^3 C}{4 \pi a^2 J},$$ (3)

where C is the concentration of the element (mol/cm^3), J is the evaporative flux of the element $(mol/cm^2/h)$, and a is the radius of the droplet (cm). The cooling time, T, is given simply by

$$T = \frac{\Delta T}{dT/dt},$$ (4)

where ΔT is the initial temperature minus the final temperature and the denominator is the cooling rate. A dimensionless parameter, R, defined as the ratio of the evaporation time to the cooling time, τ/T, is thus given by

$$R = \frac{a C \, dT/dt}{3 J \Delta T}.$$ (5)

It is expected that chemical and isotopic effects whose magnitudes depend on the degree of evaporation of the model droplets, such as the decline in the concentrations of MgO and SiO_2 in the droplets, the difference in Åk content between the cores and rims of melilite crystals, and the enrichment in heavy isotopes of Mg and Si in the droplets, will all increase as R decreases.

3.2. A Case Study

Model results for composition δ, a possible precursor of Type B2 inclusions, are shown in Figure 3 for a peak temperature of 1693 K, a cooling rate of 0.5 K/h, an initial droplet radius of 0.25 cm, and a P_{H_2} of 10^{-6} bar. Complete fractionation of melilite is assumed, as is complete equilibration of spinel that remains in contact with the liquid. The distribution of Mg between gas, liquid, melilite, and spinel is illustrated in Figure 3a as a function of temperature. At the peak temperature, 34% of the Mg is already present in spinel. Melilite begins

to crystallize at 1674 K, enclosing an ever-increasing fraction of the spinel with falling temperature. When the calculation ends at the solidus temperature, 1500 K, 39% of the original Mg is in spinel, 10% is in melilite, 25% remains in the liquid, and the other 26% has evaporated. The resulting variation of the chemical composition of the liquid is shown in Figure 3b. Before melilite crystallization, the MgO content falls due to the combined effects of Mg evaporation and spinel precipitation, SiO_2 remains constant due to the counteracting effects of its concentration by spinel removal and its loss by $SiO_{(g)}$ evaporation, Al_2O_3 remains constant due to the counteracting effects of its removal in spinel and its relative concentration by evaporation of $Mg_{(g)}$ and $SiO_{(g)}$, and CaO increases due to its relative concentration by both spinel precipitation and evaporative loss of $Mg_{(g)}$ and $SiO_{(g)}$. After melilite begins to crystallize, CaO and Al_2O_3 contents fall with decreasing temperature, as the amounts of these oxides removed in the crystallizing assemblage outweigh the degree of their enrichment in the liquid due to evaporation of the other oxides. The MgO content remains constant with falling temperature, as its enrichment in the liquid due to crystallization of a low-MgO assemblage is just balanced by its evaporation. The SiO_2 content rises with falling temperature, as its enrichment in the liquid due to crystallization of a relatively low-SiO_2 assemblage cannot be offset by the relatively small amount of $SiO_{(g)}$ that evaporates. The fractions of the initial magnesium, silicon, and oxygen that evaporate are shown as functions of temperature in Figure 3c, reaching 26, 14, and 9%, respectively, by 1500 K. Also shown as a function of temperature is the P_{Mg}/P_{SiO} ratio of the escaping vapor. This ratio rises initially and then falls after melilite begins to crystallize. This decline is a consequence of the continuous drop in the MgO/SiO_2 ratio of the evaporating liquid that occurs during melilite crystallization. Figure 3d shows the chemical and isotopic compositions of the melilite that crystallizes at each temperature. The melilite is seen to be normally zoned from $Åk_{24}$ to $Åk_{37}$. As a consequence of the increasing amounts of evaporation seen in Figure 3c, the isotopic compositions of magnesium, silicon, and oxygen in the liquid become progressively more enriched in the heavy isotopes with falling temperature, and this is expected to be recorded in the melilite. The last, most åkermanitic melilite to crystallize will have the most highly mass-fractionated isotopic compositions, reaching $F_{Mg} = 6.9$, $F_O = 2.5$, and $F_{Si} = 2.0$‰ in this case. Because of sequestration of fractionated melilite and trapped spinel that crystallized at higher temperature before so much evaporation occurred, the bulk isotopic composition of the inclusion as a whole is less mass-fractionated than the final melilite. Its composition is $F_{Mg} = 6.1$, $F_O = 2.1$, and $F_{Si} = 1.8$‰.

3.3. Factors Controlling the Degree of Evaporation

In this section, we investigate the sensitivity of the evolution of the droplets, as would be recorded in chemical and isotopic zoning of melilite, to the parameters that control R, i.e., the droplet size, cooling rate, and J, the latter via its dependence on P_{H_2}.

In the case study discussed above for evaporation of a droplet of composition δ and initial radius 0.25 cm into a pure hydrogen gas with $P_{H_2} = 10^{-6}$ bar, the predicted chemical and

Fig. 4. (a) Chemical and (b) isotopic zoning calculated for melilite in a 0.25-cm droplet of composition δ during cooling from 1693 K at the indicated rates while the droplet is undergoing evaporation into a hydrogen gas at $P_{H_2} = 10^{-6}$ bar.

isotopic zoning of melilite during cooling from 1693 K at 0.5 K/h are shown in Figure 3d. With initial composition and radius, P_{H_2} and peak temperature held constant, the effect of different cooling rates on the variation of the åkermanite content of melilite with temperature is shown in Figure 4a, and on the variation of the F_{Mg} of the melilite with its åkermanite content in Figure 4b. At the fastest cooling rate shown, 3 K/h, melilite is normally zoned, reaching $Åk_{44}$ at 1500 K (Fig. 4a), and the degree of evaporation is the least, with the last melilite crystallizing from a liquid with F_{Mg} of 1.0 (Fig. 4b). With progressively decreasing cooling rates, however, the time to cool to 1500 K becomes longer, causing the degree of evaporation to increase, so that the final melilite contains progressively less åkermanite (Fig. 4a) and progressively higher F_{Mg} (Fig. 4b). At the lowest cooling rate shown, 0.2 K/h, the degree of evaporation is so extreme that the åkermanite content decreases continuously from the first melilite to form to the last; i.e., it is reversely zoned, and the final F_{Mg} is 23.0‰. Note that the åkermanite content of the first-crystallizing melilite gradually declines with decreasing cooling rate. This is due to the increased amount of evaporation that occurs due to the longer time necessary to cool from 1693 K to melilite precipitation temperatures at the lower cooling rates. The decreasing åkermanite content of the initial melilite, in turn, causes the temperature of melilite appearance to increase.
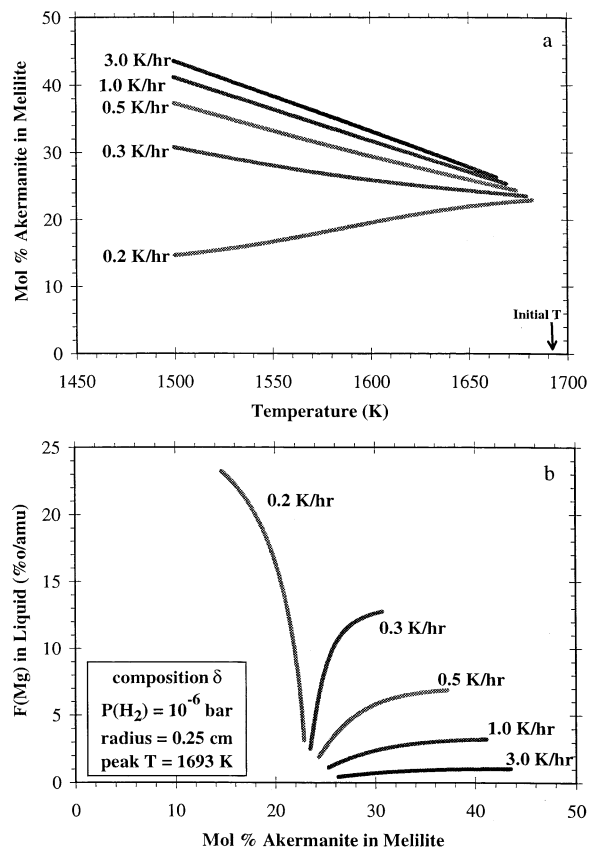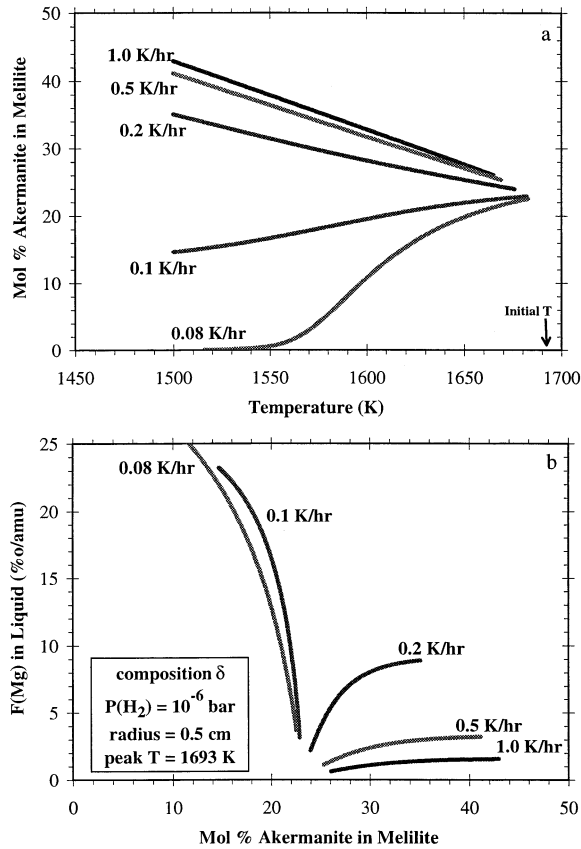
Fig. 5. (a) Chemical and (b) isotopic zoning calculated for melilite in a 0.5-cm droplet of composition δ during cooling from 1693 K at the indicated rates while the droplet is undergoing evaporation into a hydrogen gas at $P_{H_2} = 10^{-6}$ bar.
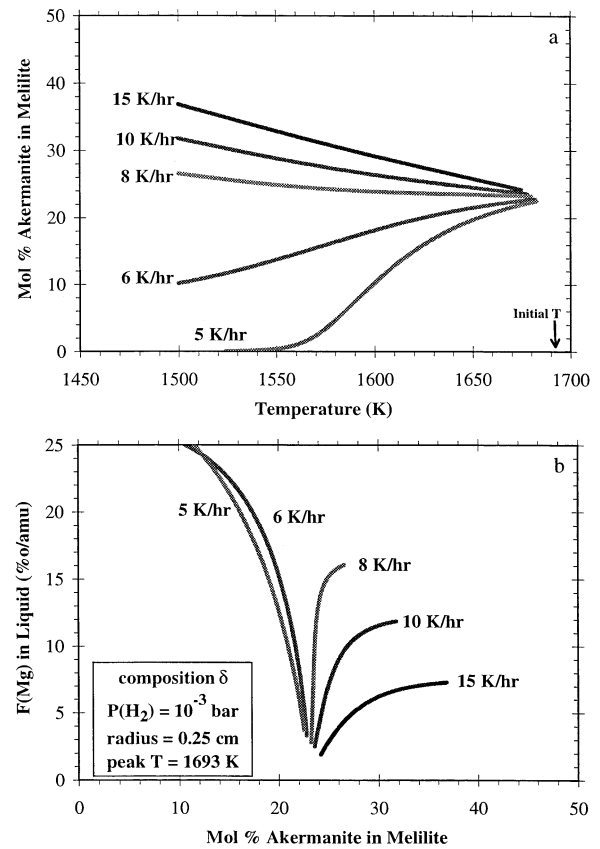
Fig. 6. (a) Chemical and (b) isotopic zoning calculated for melilite in a 0.25-cm droplet of composition δ during cooling from 1693 K at the indicated rates while the droplet is undergoing evaporation into a hydrogen gas at $P_{H_2} = 10^{-3}$ bar.

To study the effect of droplet size on the degree of evaporation, the entire calculation was repeated in an identical fashion, except that the droplet radius was doubled, from 0.25 to 0.5 cm. Results are plotted in Figures 5a and 5b. As in the previous case, both the initial and final åkermanite content of the melilite decrease, the zoning goes from normal to reverse, and the F_{Mg} of the final melilite increases with decreasing cooling rate. According to Eqn. 5, if the radius of the droplet is doubled, the parameter R, and thus the degree of evaporation, would remain constant if the cooling rate were decreased by a factor of 2 when all other variables are held constant. As expected, melilite zoning profiles in Figure 5 are very similar to those in Figure 4 but at half the cooling rate of those in Figure 4.

To study the effect of P_{H_2} on the degree of evaporation, the entire calculation was repeated in an identical fashion to the first one, except that P_{H_2} was increased by a factor of 10^3, from 10^{-6} to 10^{-3} bar. The droplet radius is 0.25 cm. Results are plotted in Figures 6a and 6b. Again, both the initial and final åkermanite content of the melilite decrease, the zoning goes from normal to reverse, and the F_{Mg} of the final melilite increases with decreasing cooling rate. Data taken from Figure 4 in Grossman et al. (2000) indicate that, relative to their values at 10^{-6} bar, both J_{Mg} and J_{SiO} increase by factors of 2.6, 8.1, and 25 as P_{H_2} increases by factors of 10, 10^2, and 10^3, respectively. Since J increases by a factor of 25 when P_{H_2} increases

from 10^{-6} to 10^{-3} bar, the degree of evaporation should remain constant if the cooling rate also increases by a factor of 25 when all other variables are held constant, according to Eqn. 5. When the profiles in Figure 6 are compared with those in Figure 4, this behavior is observed.

4. APPLICATION TO REFRACTORY INCLUSIONS

4.1. Constraints from Natural Inclusions

4.1.1. Sizes and Bulk Chemical Compositions

The objective of this section is to see if Types A and B refractory inclusions could have been derived from plausible condensate precursor compositions by melting, followed by evaporation into a pure H_2 gas during cooling and crystallization and, if so, under what physicochemical conditions.

Knowledge of the shapes and sizes of refractory inclusions comes from random sections through them that only rarely pass through their geometric centers. While a range of sizes undoubtedly exists, observations of Types A and B inclusions in CV3 chondrites suggest that 0.25 cm is a very good estimate of the most frequently encountered radius, and this value was used as the initial radius for the molten spheres modeled herein. Even in the most extremely evaporated case in this work, the final radius differs by only 7% from this initial value.
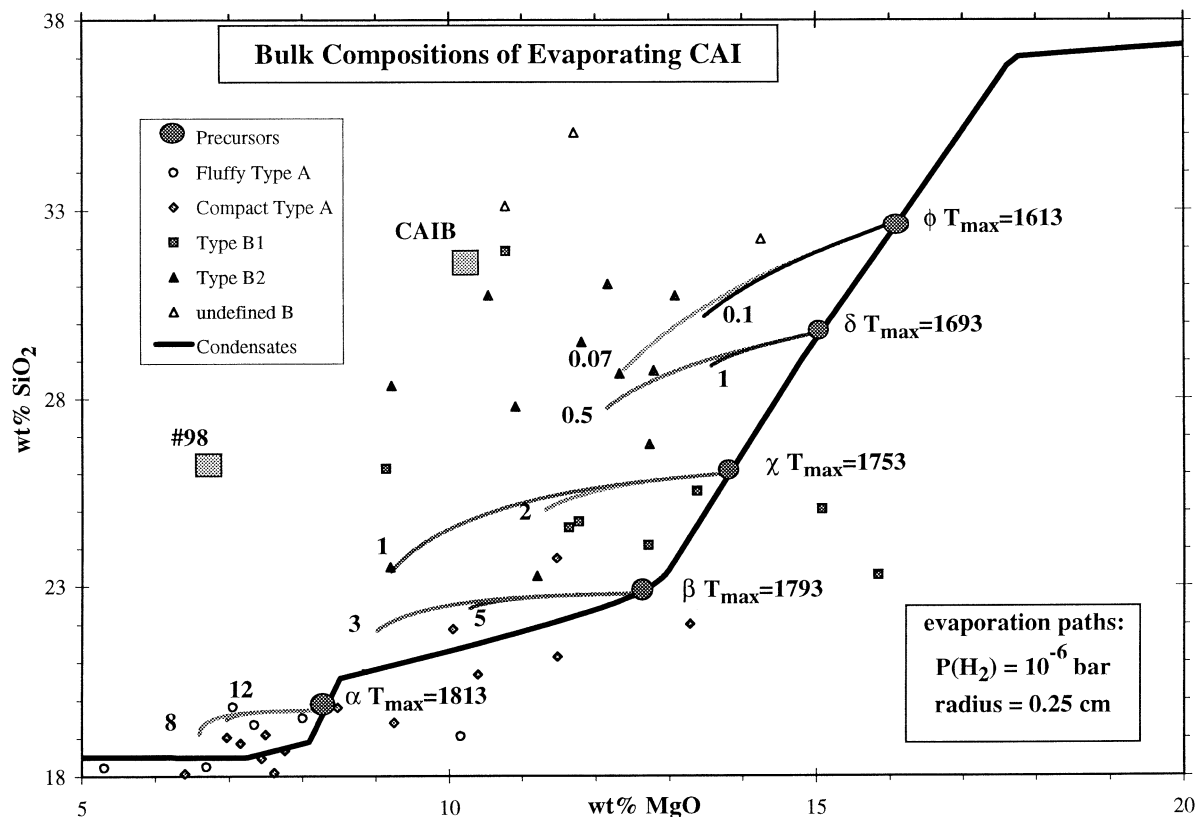
Fig. 7. Spinel-corrected bulk chemical compositions of Types A and B inclusions compared to the calculated composition variation of equilibrium high-temperature condensates from a solar gas at $P^{tot} = 10^{-5}$ bar. Compositions of condensate assemblages selected as starting materials for evaporation calculations are indicated by Greek letters, and are listed in Table 1. Curves emanating from these precursor compositions are the evolutionary paths of bulk compositions produced by evaporation of 0.25-cm droplets into 10^{-6} bar of pure H_2 during cooling to 1500 K from the peak temperatures marked "T_{max}" at the rates indicated along the curves (K/h). See text for discussion of peak temperature constraints. Large squares are the bulk compositions of CAIB and #98, whose liquid-crystal phase relations have been investigated by Stolper (1982) and Paque and Stolper (1984), respectively.

Shown in Figure 7 are the spinel-corrected bulk chemical compositions of the refractory inclusions discussed by Grossman et al. (2000), identified as fluffy Type A, compact Type A, Type B1, or Type B2 when this is known. A test of the evaporation model is to see if it can generate these bulk chemical compositions from the array of precursor compositions lying along the trajectory marked "condensates" in Figure 7.

4.1.2. Bulk Isotopic Compositions

Although both the Mg and Si isotopic compositions of only one of the inclusions plotted in Figure 7 are known, virtually all Types A and B inclusions are mass-fractionated toward the heavy isotopes of these elements, probably indicating that they have been partially evaporated. The inclusions for which both the Mg and Si isotopic compositions are known are summarized by Grossman et al. (2000), from which it is seen that F_{Mg} varies from 0 to 10.9‰ and F_{Si} from 0 to 5.2‰, indicating evaporative loss of up to 42% of the Mg and 38% of the Si. There are insufficient data to determine whether any systematic difference exists between the degree of evaporation experienced by Type A inclusions and that of Type B's. Thus, a

further test of the evaporation model is to see if it can produce the bulk chemical compositions of refractory inclusions from those of the condensate precursors while keeping F_{Mg} and F_{Si} within this observed range.

As pointed out by Clayton et al. (1977), refractory inclusions exchanged their oxygen with a reservoir near the terrestrial line subsequent to evaporation and condensation processes. Thus, any isotopic mass-fractionation of oxygen produced by evaporation must contribute to the spread of oxygen isotopic compositions measured in the slope-1/2 direction about the carbonaceous chondrite anhydrous mixing line. As pointed out by Grossman et al. (2000), when the oxygen isotopic compositions of measured inclusions are projected from plausible ^{16}O-poor reservoir compositions onto the mass-fractionation line passing through $\delta^{18}O = \delta^{17}O = -40$‰, the observed spread of ~3‰/ amu in the slope-1/2 direction expands to approximately double that amount. Thus, another constraint that successful evaporation models must satisfy is to keep F_O below ~6‰.

4.1.3. Chemical Zoning in Melilite

There are no measured magnesium, silicon, or oxygen isotopic zoning profiles of single melilite crystals to compare with

predictions of evaporation models; however, core-to-rim profiles of åkermanite contents are known for several melilite crystals from each of many compact Type A and Type B1 inclusions (e.g., Podosek et al., 1991). Few profiles exist for fluffy Type A and Type B2 inclusions. Although it is difficult to select a single melilite zoning profile as most representative of the myriad distinct patterns in a single inclusion type, the profiles do provide additional constraints for evaporation models. What is obtained from the model is the åkermanite content as a function of the fraction of the total volume of melilite crystallized, and assumptions must be made about how to convert one-dimensional profiles of åkermanite vs. distance from the center of a real melilite crystal into these units. We assume that each profile used for this purpose passes through the center of the crystal, that the length and width of the crystal in the plane of the thin section are the true dimensions of the crystal, that the third dimension is equal to the shorter of the two dimensions in the plane of the section, that the volume of the crystal is the product of the three dimensions, and that the relative dimensions are constant during growth. This allows the fraction of the total melilite crystal volume to be calculated as the cube of the fractional distance along the zoning profile.

Crystallization of Types A and B inclusions from silicate liquids is usually discussed with reference to the liquid-crystal phase relations in that part of the CMAS system projected from spinel onto the gehlenite-forsterite-anorthite plane. The phase relations in the gehlenite-rich corner of this diagram are reproduced in Figure 2. Grossman et al. (2000) showed that spinel-corrected bulk chemical compositions of both Type A and Type B inclusions plot in the melilite field, which means that spinel and melilite are the first phases to crystallize. With falling temperature, the liquid lines of descent eventually reach the melilite-anorthite boundary or cotectic, where anorthite begins to cocrystallize with spinel and melilite at equilibrium. As the temperature continues to fall, the liquid composition travels along this cotectic to the fassaite field, where the liquid disappears into spinel + melilite + anorthite + fassaite. The reason why Type B's contain so much more fassaite than Type A's is that the bulk compositions of the Type B's plot so much closer to the fassaite field than those of the Type A's, as seen in Stolper (1982). The model presented here ignores crystallization of anorthite and fassaite, which are assumed to precipitate from whatever liquid remains at the solidus at 1500 K. Thus, the model fails to account for the effects of crystallization of these phases on the liquid composition and consequently on the composition of the cocrystallizing melilite. Because anorthite and fassaite crystallize from the very last dregs of liquid, however, this simplification affects the calculated composition of only the very outermost layers of the melilite crystals.

4.1.4. Cooling Rates of Type B Inclusions

In dynamic crystallization experiments performed on composition CAIB, MacPherson et al. (1984) discovered that, at relatively high cooling rates, anorthite fails to precipitate at its equilibrium crystallization temperature, and fassaite crystallizes before anorthite. Melilite crystals grown before precipitation of fassaite are normally zoned. With the onset of crystallization of fassaite in the absence of anorthite, however, the Al/Mg ratio of the liquid rises steeply, causing the cocrystal-

lizing melilite to increase its gehlenite content with falling temperature, resulting in formation of reversely zoned mantles on the preexisting, normally zoned melilite cores. Suppression of the anorthite crystallization temperature to below that of fassaite, and consequent production of reversely zoned melilite bands, occurred in experiments cooled at 0.5 to 20 K/h. Although anorthite suppression occurs at 50 K/h, reversely zoned bands were not observed, presumably because fassaite formed at such high cooling rates is much more aluminous than that at lower cooling rates. The widespread occurrence of reversely zoned bands toward the outsides of melilite crystals in Types B1 and B2 inclusions is taken as evidence that they crystallized while cooling at rates below 50 K/h and above that at which anorthite crystallizes at its equilibrium temperature, somewhere below 0.5 K/h. Thus, successful evaporation models for Type B inclusions must produce their bulk chemical and isotopic compositions within this range of cooling rates.

4.2. Type A Inclusions

4.2.1. General

Most Type A inclusions, fluffy and compact, plot in a tight cluster at 7 to 8% MgO and 18 to 20% SiO_2 in Figure 7, while others stretch out along the condensation curve toward 13% MgO and 23% SiO_2. Several of the latter plot close to, but below, the condensation curve in a region that cannot be reached by evaporation of compositions along the curve, but it must be emphasized that there are uncertainties in the measurement of their bulk compositions and that the data have also been subjected to a rather large spinel correction (Grossman et al., 2000). Most of the Type A's plot so close to the condensation curve that it may seem unnecessary to derive their compositions from precursors along the curve. Even an inclusion plotting so close to α as one with, say, 7% MgO and 19% SiO_2, however, could be a residue of α that resulted from evaporation of ~12% of its MgO and ~3% of its SiO_2. Furthermore, the summary of isotopic data in Grossman et al. (2000) shows that one of the two Type A inclusions whose Mg and Si isotopic compositions have been measured appears to have lost 22% of its MgO and 12% of its SiO_2, while the other has lost 25% of its MgO and 20% of its SiO_2, implying that the Type A's have definitely undergone significant evaporation.

For all compositions discussed in this paper, spinel is the liquidus phase, i.e., the first to crystallize from a melt upon equilibrium cooling in a closed system. Experiments on two synthetic compositions plotted in Figure 7, CAIB (Stolper, 1982), and #98 (Paque and Stolper, 1984) show similar liquidus temperatures, 1823 and 1810 K, respectively, but the temperature at which melilite begins to crystallize is much higher, 1783 K, for #98, the composition closer to the Type A field, than for CAIB, 1675 K. Similarly, calculated temperatures of melilite appearance rise steeply as bulk MgO and SiO_2 contents decrease, reaching ~1800 K for α and β. For #98, Paque and Stolper (1984) found that dendritic or feathery melilite crystals formed whenever peak temperatures were near or above the liquidus, at all cooling rates between 0.5 and 1000°C/h. From the absence of such textures in natural Type A inclusions, it can be concluded that their peak temperatures were below the liquidus. In a petrographic and mineral-chemical study of com-

pact Type A inclusions, Simon et al. (1999) found some melilite crystals whose long axes are at high angles to the outer edges of their host inclusions, and whose åkermanite contents increase along their lengths toward the inclusion interiors, indicating that melilite nucleated on the surfaces of melt droplets and grew inward with falling temperature. Simon et al. (1999) found evidence for relict melilite crystals in only one inclusion, and concluded that melilite grains in most compact Type A's crystallized from their host melt droplets, implying that peak temperatures were at or slightly above the temperature of first crystallization of melilite.

4.2.2. Fluffy Type A's

At such high peak temperatures, the partial pressures and evaporation coefficients for $Mg_{(g)}$ and $SiO_{(g)}$ are very high, resulting in very high evaporation rates, as seen from Eqn. 1 and 2. When such large values of J are coupled with the very large temperature interval, ΔT, between melilite appearance and the solidus, Eqn. 5 requires rapid cooling rates to prevent massive evaporation. When a 0.25-cm droplet of composition α cools from 1813 K at $P_{H_2} = 10^{-6}$ bar, melilite begins crystallizing at 1800 K. Figure 7 shows that a cooling rate of 8 K/h generates a final bulk composition only slightly poorer in MgO than those in the Type A cluster. The final bulk F_{Mg}, F_{Si} and F_O are 4.9, 0.5, and 0.8‰. At this cooling rate, the melilite starts out normally zoned from $Åk_6$ to $Åk_{15}$ and thereafter becomes reversely zoned to $Åk_0$. Although reverse zoning in this composition range is a characteristic of melilite crystals in fluffy Type A inclusions (MacPherson and Grossman, 1984), such crystals do not possess normally zoned cores. Rather, the reverse zoning begins in the cores of the natural crystals and extends all the way to their rims. Furthermore, the central composition is usually slightly more åkermanitic than $Åk_{20}$, considerably more magnesian than the initial melilite produced by evaporation of α. Use of lower initial peak temperatures would produce melilite with higher initial åkermanite contents, but this melilite would be stable at the peak temperature, and therefore relict. Another way of producing higher initial åkermanite contents is by evaporating more magnesian bulk compositions. For example, when a 0.25-cm droplet of composition χ cools from 1753 K at 0.5 K/h at $P_{H_2} = 10^{-6}$ bar, the resulting bulk chemical composition lies within the Type A cluster. In this case, melilite begins crystallizing at 1745 K. It will not have a normally zoned core but will be reversely zoned from $Åk_{16}$ to $Åk_0$. Given that the melilite solution model employed herein underestimates åkermanite contents by several mol.% in this composition range (Table 1), this central åkermanite content is within error of the observed value. The problem with this alternative is that so much evaporation occurs that the final bulk F_{Mg} is 16.2‰, far beyond the maximum so far observed in refractory inclusions. Thus, unless the cores of the melilite crystals in fluffy Type A inclusions are relict, there may be no way to generate their chemical and isotopic compositions by the process envisioned in this work. Indeed, MacPherson and Grossman (1984) argued that these objects were never molten and cannot be volatilization residues, on the basis of their reversely zoned melilite, the variation of their spinel compositions, and their nodular structures.
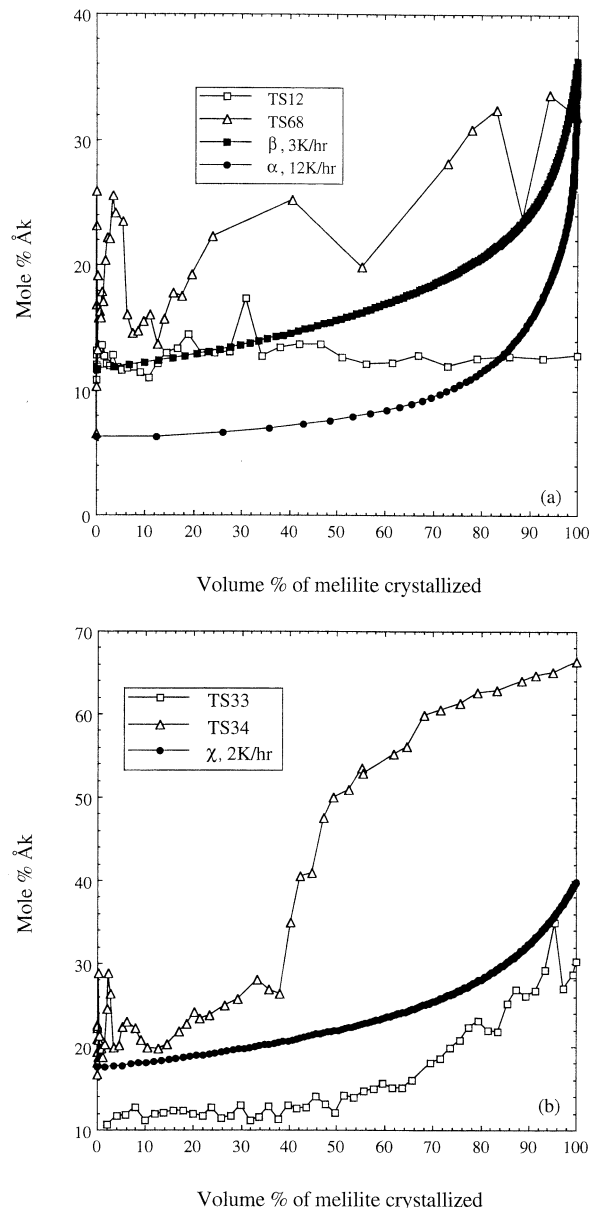

Fig. 8. Chemical zoning profiles calculated for melilite crystals (a) during evaporation of potential precursors of Type A inclusions, compared with profiles observed in compact Type A inclusions; and (b) during evaporation of potential precursors of Type B inclusions, compared with profiles observed in Type B1 inclusions.

4.2.3. Compact Type A's

Figure 7 shows that, when a 0.25-cm droplet of composition α cools from 1813 K at 12 K/h at $P_{H_2} = 10^{-6}$ bar, a bulk chemical composition within the Type A cluster is produced. The final bulk F_{Mg}, F_{Si}, and F_O are 3.8, 0.4, and 0.6‰, respectively, within the observed range. At this cooling rate, the melilite is normally zoned from $Åk_6$ to $Åk_{36}$. In Figure 8a, the calculated zoning profile is compared with examples of two profiles, labeled TS12 and TS68, commonly encountered in compact Type A inclusions. It is a good match for neither. The initial åkermanite content of the calculated profile is lower than

those of TS12 and TS68, $Åk_{13}$ and $Åk_{16}$, respectively. While the calculated profile remains flat out to >50 vol.% crystallized and then rises steeply in the outermost 20%, TS12 stays flat, and TS68 has a very jagged, nonuniform beginning with a steep rise starting at 50% crystallized. Although these two profiles come from different inclusions, the differences between them are comparable to those between different crystals within a single compact Type A inclusion. Such differences, together with the irregularities seen along individual profiles, are evidence that individual crystals undergo changes in growth rate and that different crystals solidifying from the same melt nucleate at different temperatures and experience different liquid compositions depending on the number and mineralogical identities of other crystals in their immediate vicinities. What is calculated, on the other hand, is a model zoning profile for a statistically average crystal, based on the assumption that the amount of melilite that crystallizes in any temperature interval is the amount predicted by liquid-crystal equilibrium. All in all, the evaporation residue produced by cooling of α at 12 K/h can be considered a reasonable match for some compact Type A inclusions.

Many other initial compositions lying along the condensation trajectory between α and β are capable of evolving into evaporation residues similar in composition to those in the Type A cluster by cooling from ~1800 K at ~2 to 6 K/h at $P_{H_2} = 10^{-6}$ bar. Figure 7 shows that, at 3 and 5 K/h, evaporation of a 0.25-cm droplet of composition β produces bulk chemical compositions close to those of the more SiO_2-rich Type A's. At 5 K/h, final bulk F_{Mg}, F_{Si}, and F_O are 4.8, 0.6, and 1.0‰, respectively, and the melilite, which begins crystallizing at 1777 K, is normally zoned from $Åk_{12}$ to $Åk_{47}$. At 3 K/h, the bulk F_{Mg}, F_{Si}, and F_O are 7.8, 1.2, and 1.7‰, respectively, and the melilite is normally zoned from $Åk_{12}$ to $Åk_{36}$, as shown in Figure 8a. These isotopic compositions are all well within the observed ranges. At 2 K/h, however, the bulk F_{Mg}, 11.1‰, exceeds the highest observed value of 10.9‰.

Because evaporation rates increase with increasing P_{H_2}, faster cooling rates will produce very similar evaporation effects at higher P_{H_2}. Thus, compositions within the Type A cluster can be produced by evaporation of initial compositions lying between α and β at cooling rates of 5 to 16 K/h at $P_{H_2} = 10^{-5}$ bar, 16 to 49 K/h at $P_{H_2} = 10^{-4}$ bar, etc.

4.3. Type B Inclusions

4.3.1. General

All Type B inclusions contain major amounts of fassaitic pyroxene and significant anorthite, in addition to melilite and spinel. While Type B1 and Type B2 inclusions are mineralogically similar, the B1's differ from the B2's in being concentrically zoned, with nearly monomineralic mantles of melilite. As in some compact Type A inclusions, long axes of these melilite crystals are at high angles to the outer edges of their host inclusions, and their åkermanite contents increase along their lengths toward inclusion interiors, indicating that melilite nucleated on the surfaces of melt droplets and grew inward with falling temperature (MacPherson and Grossman, 1981). Figure 7 shows that, with the exception of one very high-SiO_2 outlier, spinel-corrected Type B1 inclusion compositions plot within a narrow band of SiO_2 contents, from 23 to 26 wt.%, sandwiched between the lower-SiO_2 Type A's and the higher-SiO_2 Type B2's.

In their dynamic crystallization experiments on CAIB, a Type B–like composition, Stolper and Paque (1986) found that dendritic melilite crystals resulted from peak temperatures above the liquidus, 1823 K, and that anorthite did not crystallize when peak temperatures were above 1723 K, for all cooling rates between 2 and 1000°C/h. Because Type B inclusions do not contain dendritic melilite but do contain anorthite, and because their minimum åkermanite contents are typically in the same range as those found in experiments with peak temperatures near that for melilite entry, 1673 K for CAIB, Stolper and Paque (1986) concluded that Type B inclusions reached peak temperatures within 20 K of the temperature at which melilite first crystallizes. In the present study, therefore, melilite crystallization within 20 K of the peak temperature is adopted as a constraint for Type B inclusions.

4.3.2. Type B1's

Composition χ is an appropriate precursor for Type B1 inclusions. When a 0.25-cm droplet of this composition is cooled at 2 K/h from a peak temperature of 1753 K at $P_{H_2} = 10^{-6}$ bar, melilite, $Åk_{17}$, begins to crystallize at 1740 K and the bulk chemical composition evolves into the middle of the field of Type B1's. The final bulk F_{Mg}, F_{Si}, and F_O are 5.1, 1.1, and 1.4‰, respectively, well within the ranges observed for refractory inclusions. The calculated melilite zoning profile is shown in Figure 8b, along with examples of two frequently encountered profiles in natural Type B1 inclusions, TS33 and TS34. MacPherson et al. (1984) reported that the normally zoned cores of melilite crystals in Type B1's reach ~$Åk_{70}$ before the onset of pyroxene crystallization causes precipitation of the reversely zoned bands on top of them. Thus, the similarity between the calculated profile and TS33 is spurious, as the final åkermanite content of TS33, $Åk_{30}$, is obviously from a grain that stopped crystallizing well before fassaite precipitation, while the model calculation is supposed to predict the composition variation all the way to the solidus temperature, by which point fassaite should have precipitated. Because TS34 reaches a final composition of $Åk_{66}$, it is a more appropriate profile to compare with the calculated one. Although beginning with the same åkermanite content as the calculated profile, however, TS34 begins to rise sharply after 40 vol.% crystallized, while the calculated profile rises steeply only in the final 20% of crystallization and reaches a final composition of $Åk_{40}$, falling far short of the final åkermanite content of TS34. This discrepancy may be due to inaccuracy of the melilite solution model. In Figure 2, note that the experimentally determined liquid line of descent from CAIB, a Type B–like bulk composition, curves more sharply to the left at lower temperature than the computed one. The melilite composition crystallizing instantaneously may be found by drawing the tangent to such a curve at the liquid composition of interest and finding its intersection with the melilite composition line along the gehlenite-forsterite axis. Because the calculated liquid line of descent curves much less than the experimentally determined one, calculated melilite compositions never reach åkermanite contents as high as those found in experiments at the low temperatures immediately

above the fassaite crystallization temperature. Cooling χ at 2 K/h at $P_{H_2} = 10^{-6}$ bar produces evaporation residues whose bulk chemical, bulk isotopic, and mineralogical properties can thus be considered a good match for those of Type B1 inclusions.

As seen in Figure 7, at a cooling rate of 1 K/h, final bulk chemical compositions much further from χ can be reached, while the melilite remains normally zoned to $Åk_{29}$ and the final bulk F_{Mg}, F_{Si}, and F_O rise to 10.2, 2.4, and 2.7‰, respectively. Slightly slower cooling rates will produce F_{Mg} beyond the maximum observed value, but even at 1 K/h, the final åkermanite content is much lower than observed in most Type B1 inclusions. Thus, evaporation of compositions similar to χ at $P_{H_2} = 10^{-6}$ bar will produce objects similar to Type B1 inclusions at 1.5 to 3 K/h, but not at 1 K/h. Again, at higher P_{H_2}, faster cooling rates are allowed. At $P_{H_2} = 10^{-4}$ bar, for example, cooling χ at rates from ~12 to ~24 K/h would produce similar evaporation effects as those illustrated in Figure 7. At 10^{-3} bar, this would be achieved at cooling rates from 38 to 75 K/h. Because it is not known whether cooling rates of >20 K/h can produce fassaite precipitation-induced melilite zoning reversals, however, formation of Type B1 inclusions by the mechanism discussed herein may be precluded at 10^{-3} bar.

4.3.3. Type B2's

The precursors of most Type B2 inclusions were probably more MgO- and SiO$_2$-rich than composition χ. When composition δ, for example, is cooled from 1693 K at 0.5 K/h at $P_{H_2} = 10^{-6}$ bar, its composition evolves into the relatively low-SiO$_2$, high-MgO portion of the field of Type B2 inclusions. Under these conditions, melilite begins crystallizing at 1674 K, and is normally zoned from $Åk_{24}$ to $Åk_{38}$. An inclusion formed in this way would have bulk F_{Mg}, F_{Si}, and F_O of 6.1, 1.8, and 2.1‰, respectively.

Generally, Type B2 inclusions with SiO$_2$ contents lying above the evaporation curves emanating from δ require precursors more SiO$_2$-rich than δ, such as ϕ. A peak temperature of 1613 K assures melilite crystallization from ϕ within 20 K of the peak temperature. When a 0.25-cm droplet of this composition is cooled at 0.07 K/h at $P_{H_2} = 10^{-6}$ bar, melilite is normally zoned from $Åk_{24}$ to $Åk_{31}$, and the final bulk F_{Mg}, F_{Si}, and F_O will be 8.2, 3.0, and 3.3‰, respectively. It is not known whether such a slow cooling rate would suppress anorthite nucleation, thereby generating the reversely zoned melilite bands seen experimentally by MacPherson et al. (1984). As shown by the 0.1 K/h evaporation path at the same P_{H_2}, however, faster cooling rates than this produce insufficient evaporation to reach the compositions of Type B2 inclusions because the peak temperature is only 113 K above the solidus. Because of the increase in evaporation rate with increasing P_{H_2}, the same bulk composition change produced along the 0.07 K/h path at 10^{-6} bar in Figure 7 can be generated at a P_{H_2} of 10^{-3} bar, for example, but at ~1.8 K/h, a cooling rate sufficiently fast to ensure anorthite-suppression-induced reverse zoning.

While such evaporation conditions and those illustrated for composition δ could produce residues having the compositions of those Type B2 inclusions with 12 to 15 wt.% MgO and 26 to 30 wt.% SiO$_2$, it seems unlikely that those having between 27 and 35 wt.% SiO$_2$ at MgO < 12 wt.% can be produced as

evaporation residues of precursor compositions along this condensation curve. There are two reasons for this. First, precursors more SiO$_2$-rich than ϕ are needed to produce these relatively SiO$_2$-rich inclusions, but the slope of the condensation curve in this region is such that precursors of the required SiO$_2$ contents also have higher MgO contents than ϕ. The difference in MgO content between such precursors and the inclusions in question increases with the SiO$_2$ content of the precursors, requiring an ever-increasing degree of Mg evaporation to reach the inclusion compositions. The second reason is that, as the MgO and SiO$_2$ contents of the precursor compositions increase, the slopes of the evaporation paths steepen; i.e., a greater degree of SiO$_2$ evaporation occurs for the same amount of MgO evaporation as the precursor becomes more MgO- and SiO$_2$-rich. As a result, evaporation conditions have not been found that can produce the relatively SiO$_2$-rich Type B's from precursor compositions along the illustrated condensation curve without exceeding the maximum observed F_{Mg}. This suggests that a more appropriate condensation curve would be one whose SiO$_2$ rises more steeply with MgO above 15% MgO, but such a curve has not yet been predicted.

4.4. Isotopic Zoning of Melilite

Another prediction of the evaporation model is that any melilite crystal that grew continuously with falling temperature should be isotopically zoned because successively formed layers of the crystals grew from progressively more evaporated and isotopically mass-fractionated liquid. The evaporation model can be tested by making measurements of isotopic zoning on crystals that have not been recrystallized or overprinted by the effects of secondary alteration, using microbeam instruments of appropriate sensitivity. Figure 9 shows the correspondence between chemical and magnesium isotopic zoning in melilite crystals predicted to form along six of the evaporation paths shown in Figure 7. Despite wide crystal-to-crystal variations in chemical zoning profiles seen within individual inclusions and systematic errors in predicted åkermanite contents alluded to above, Figure 9 can be used as an approximate guide to the magnitudes of possible isotope effects and the thicknesses of zones to which they apply. The largest mass-fractionations are, of course, found in the outermost zones of the crystals, but the thicknesses of the zones enriched in heavy isotopes vary with starting composition, cooling rate and crystal size. Those paths for which the degree of evaporation is greatest yield melilite with the largest mass-fractionations of Mg and other elements. On this figure, the volume fraction of melilite crystallized is converted to the radius of a hypothetical, 250-μm spherical crystal. Smaller crystals formed under identical conditions will have thinner zones at a particular average isotopic composition, and larger crystals will have thicker zones. Fassaite and anorthite crystallize from the last liquids to disappear, and therefore from the most mass-fractionated ones. Whether these phases are more isotopically fractionated than the outermost measurable layers of the melilite crystals in the same inclusion depends on what fraction of the total melilite crystallized after the beginning of precipitation of fassaite and anorthite.
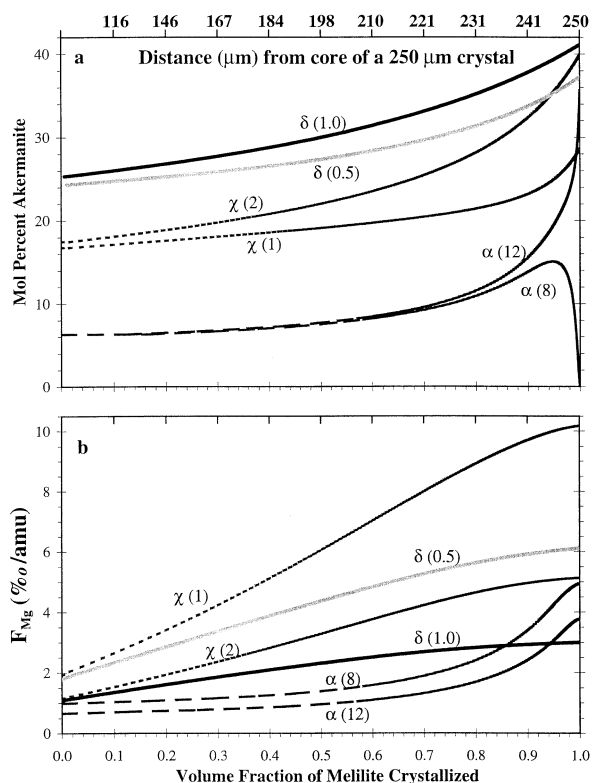
Fig. 9. (a) Chemical and (b) Mg isotopic zoning predicted for melilite crystals that form along some of the evaporation paths in Figure 7. Curves are labeled with Greek letters and numbers corresponding to initial compositions and cooling rates, respectively, in Figure 7. The volume fraction of melilite is converted to the radius of a hypothetical, 250-μm spherical melilite crystal.

4.5. Limitations

Throughout this work, the amounts and compositions of phases crystallizing in a given temperature interval are assumed to be those given by liquid-crystal equilibrium, even as previously formed crystals are assumed to be out of equilibrium with the liquid. The variability of melilite zoning patterns found within individual inclusions has been cited above as evidence for nonequilibrium crystallization, a factor that may have also caused violation of the assumption that all of the investigated liquids disappeared at the equilibrium solidus temperature of 1500 K. In dynamic crystallization experiments conducted at cooling rates of 0.5 to 50 K/h, MacPherson et al. (1984) found persistence of liquids to temperatures as low as 1373 K. Even if this is a kinetic effect due to fast cooling rates, the similarity of these rates to those found in the present study suggests that the assumption that all liquid disappeared at 1500 K may be incorrect, and may have caused the model to underestimate the extent of evaporation. On the other hand, the ubiquitous spinel layer on the surface of the inclusions and textural evidence that melilite preferentially nucleated on the edges of the melt droplets that became compact Type A and Type B1 inclusions suggests that the surfaces of many of these melt droplets may have become crowded with crystals early in the cooling history. Failure of the present model to consider the effect of this reduction of the surface area of liquid actually exposed to the

gas may result in an overestimate of the magnitude of evaporation effects.

In this work, the only combinations of starting composition and cooling rate considered appropriate for forming refractory inclusions are those that simultaneously yield bulk chemical and isotopic compositions, and melilite zoning profiles, consistent with those observed in real inclusions. Even for the evaporation conditions discussed above that pass these tests, however, the final bulk F_{Si} seems low relative to F_{Mg} when compared to the isotopic compositions of the inclusions summarized in Grossman et al. (2000). F_{Si} gradually increases from ~1.5‰ to 3.5‰ as F_{Mg} increases from ~3‰ to 7‰ in the latter group of inclusions. All of the final F_{Si} values predicted in this work for this range of F_{Mg} are between 0.4 and 1.8‰, however, suggesting that ~10% more of the silicon evaporated during formation of the actual inclusions than is predicted by this model. Use of the α_{SiO}/α_{Mg} ratio found in vacuum experiments instead of the ratio used here from hydrogen experiments would only increase this discrepancy. Perhaps the discrepancy is due to the inability of the model to produce evaporation residues with compositions like those of the relatively SiO_2-rich Type B2 inclusions. Such objects require evaporation of more SiO_2-rich precursors for which the ratio of the amount of SiO_2 evaporated to the amount of MgO evaporated is always greater than for the more SiO_2-poor precursors from which the successful evaporation paths arise.

Examination of Figure 7 reveals a steady decline in cooling rates at constant P_{H_2} and droplet size with increasing MgO and SiO_2 content of inclusion precursors. This is a consequence of the petrologic constraint that peak temperatures were close to the temperatures of incoming of melilite, and that the latter decline with increasing MgO and SiO_2 content, while the solidus temperature remains constant. Because of the limited number of inclusions for which both F_{Mg} and F_{Si} data exist, no distinction can be made in the degree of evaporation between different inclusion types. As seen from Eqn. 5, for the degree of evaporation to remain the same while the temperature interval decreases, the cooling rate must decline with increasing MgO and SiO_2 content.

MacPherson and Davis (1993) and Beckett et al. (2000) observed that the Na and åkermanite contents of the åkermanite-rich portions of melilite crystals in some Type B refractory inclusions are correlated. This suggests that Na, a volatile element, was present in the liquids from which these portions of the melilite crystals precipitated, implying that the melting event recorded by this melilite occurred after secondary alteration had begun to introduce Na into the inclusions, and that total evaporative loss of Na had not occurred before the åkermanite-rich portions of the melilite crystals solidified. It is very difficult to imagine melting at conditions that caused tens of percent of Mg and Si to evaporate without total loss of Na. This leads to the possibilities that Mg and Si loss occurred in a melting event that predated the one in which Na was present, and that the latest melting event erased Mg isotopic zoning of melilite crystals that should have been produced by progressive Mg volatilization during their growth in the earlier melting event. If the above interpretation of the Na-åkermanite correlation is correct, the isotopic zoning predicted for melilite in this work may not be present in the high-åkermanite portions of melilite grains in which this correlation is found.

This discussion focuses attention on the need for a complete study of at least several whole, unaltered inclusions to test the evaporation model proposed here. Indeed, the bulk chemical composition is known for only one of the inclusions whose bulk F_{Mg} and F_{Si} are known. In such a study, inclusions of different types must be extracted whole to measure their sizes accurately. An experimental protocol must be developed so that bulk chemical and bulk magnesium, silicon, and oxygen isotopic analyses can be made of truly representative samples, while preserving sufficient material for thin sections in which chemical and isotopic zoning can be measured within individual crystals.

There is also a need to determine the effect on compositions of evaporation residues of elements in the gas phase in addition to hydrogen.

5. CONCLUSIONS

The sequence of equilibrium condensate assemblages predicted to form during falling temperature in a solar gas at 10^{-5} bar total pressure produces a series of bulk chemical compositions that are suitable precursors for compact Type A and Type B1 inclusions in CV3 chondrites. When these assemblages are partially melted in pure hydrogen at peak temperatures in the vicinity of the initial crystallization temperature of melilite, the relative amounts of MgO and SiO_2 that evaporate during subsequent cooling and crystallization are such that the bulk chemical compositions evolve into the composition fields of refractory inclusions, mass-fractionated isotopic compositions of Mg, Si, and O are produced that are in the range of the isotopic compositions of natural inclusions, and melilite zoning profiles result that are similar to those observed in real inclusions. For droplets of radius 0.25 cm evaporating at $P_{H_2} = 10^{-6}$ bar, precursors containing 8 to 13 wt.% MgO and 20 to 23% SiO_2 evolve into objects similar to compact Type A inclusions at cooling rates of 2 to 12 K/h, depending on the precise starting composition. Precursors containing 13 to 14 wt.% MgO and 23 to 26% SiO_2 evolve into objects with the characteristics of Type B1 inclusions at cooling rates of 1.5 to 3 K/h. The relatively SiO_2-poor members of the Type B2 group can be produced from precursors containing 14 to 16 wt.% MgO and 27 to 33% SiO_2 at cooling rates of <1 K/h. Type B2's containing 27 to 35 wt.% SiO_2 and <12% MgO require precursors with higher SiO_2/MgO ratios at MgO > 15% than are found on this or any other condensation curve. The characteristics of fluffy Type A inclusions, including their reversely zoned melilite, can only be understood in the context of this model if they contain relict melilite. Evaporation at higher P_{H_2} allows higher cooling rates than at 10^{-6} bar, by factors of 2.6, 8.1, and 25 at 10^{-5}, 10^{-4}, and 10^{-3} bar, respectively, for droplets of the same size. At constant P_{H_2}, the required cooling rates are inversely proportional to droplet size.

REFERENCES

Beckett J. R. (1986) *The origin of calcium-aluminum-rich inclusions from carbonaceous chondrites: An experimental study.* Ph.D. thesis, University of Chicago.

Beckett J. R., Simon S. B., and Stolper E. (2000) The partitioning of Na between melilite and liquid: Part II. Applications to Type B inclusions from carbonaceous chondrites. *Geochim. Cosmochim. Acta* **64**, 2519–2534.

Berman R. G. (1983) *A thermodynamic model for multicomponent melts, with application to the system CaO-MgO-Al$_2$O$_3$-SiO$_2$.* Ph.D. thesis, University of British Columbia.

Berman R. G. (1988) Internally-consistent thermodynamic data for minerals in the system Na$_2$O-K$_2$O-CaO-MgO-FeO-Fe$_2$O$_3$-Al$_2$O$_3$-SiO$_2$-TiO$_2$-H$_2$O-CO$_2$. *J. Petrol.* **29**, 445–522.

Charlu T. V., Newton R. C., and Kleppa O. J. (1981) Thermochemistry of synthetic Ca$_2$Al$_2$SiO$_7$ (gehlenite)-Ca$_2$MgSi$_2$O$_7$ (åkermanite) melilites. *Geochim. Cosmochim. Acta* **45**, 1609–1617.

Clayton R. N., Onuma N., Grossman L., and Mayeda T. K. (1977) Distribution of the pre-solar component in Allende and other carbonaceous chondrites. *Earth Planet. Sci. Lett.* **34**, 209–224.

Davis A. M., Hashimoto A., and Richter F. M. (1998) Isotopic mass fractionation under solar nebular conditions. *Meteoritics Planet. Sci.* **33**, A39.

Ghiorso M. S. and Sack R. O. (1995) Chemical mass transfer in magmatic processes IV. A revised and internally consistent thermodynamic model for the interpolation and extrapolation of liquid-solid equilibria in magmatic systems at elevated temperatures and pressures. *Contrib. Mineral. Petrol.* **119**, 197–212.

Grossman L., Ebel D. S., Simon S. B., Davis A. M., Richter F. M., and Parsad N. M. (2000) Major element chemical and isotopic compositions of refractory inclusions in C3 chondrites: The separate roles of condensation and evaporation. *Geochim. Cosmochim. Acta* **64**, 2879–2894.

Kuroda D. and Hashimoto A. (2000) The reaction of forsterite with hydrogen-its apparent and real temperature dependences. In *Antarctic Meteorites XXV*, pp. 64–66. National Institute of Polar Research, Tokyo, Japan.

Lange R. A. and Carmichael I. S. E. (1987) Densities of Na$_2$O-K$_2$O-CaO-MgO-FeO-Fe$_2$O$_3$-Al$_2$O$_3$-TiO$_2$-SiO$_2$ liquids: New measurements and derived partial molar properties. *Geochim. Cosmochim. Acta* **51**, 2931–2946.

MacPherson G. J. and Grossman L. (1981) A once-molten, coarse-grained, Ca-rich inclusion in Allende. *Earth Planet. Sci. Lett.* **52**, 16–24.

MacPherson G. J. and Grossman L. (1984) "Fluffy" Type A Ca-, Al-rich inclusions in the Allende meteorite. *Geochim. Cosmochim. Acta* **48**, 29–46.

MacPherson G. J. and Davis A. M. (1993) A petrologic and ion microprobe study of a Vigarano Type B refractory inclusion: Evolution by multiple stages of alteration and melting. *Geochim. Cosmochim. Acta* **57**, 231–243.

MacPherson G. J., Paque J. M., Stolper E., and Grossman L. (1984) The origin and significance of reverse zoning in melilite from Allende Type B inclusions. *J. Geol.* **92**, 289–305.

Morioka M. and Nagasawa H. (1991) Diffusion in single crystals of melilite: II. Cations. *Geochim. Cosmochim. Acta* **55**, 751–759.

Osborn E. F. and Schairer J. F. (1941) The ternary system pseudowollastonite-åkermanite-gehlenite. *Am. J. Sci.* **239**, 715–763.

Paque J. M. and Stolper E. (1984) Crystallization experiments on a range of Ca-Al-rich inclusion compositions. In *Lunar Planet. Sci. XV*, pp. 631–632. Lunar and Planetary Institute, Houston, TX.

Podosek F. A., Zinner E. K., MacPherson G. J., Lundberg L. L., Brannon J. C., and Fahey A. J. (1991) Correlated study of initial ^{87}Sr/^{86}Sr and Al-Mg isotopic systematics and petrologic properties in a suite of refractory inclusions from the Allende meteorite. *Geochim. Cosmochim. Acta* **55**, 1083–1110.

Richter F. M., Davis A. M., Ebel D. S., and Hashimoto A. (in press) Elemental and isotopic fractionation of Type B CAIs: Experiments, theoretical considerations, and constraints on their thermal evolution. *Geochim. Cosmochim. Acta*.

Robie R. A., Hemingway B. S., and Fisher J. R. (1978) *Thermodynamic Properties of Minerals and Related Substances at 298.15 K and 1*

Bar (10⁵ Pascals) Pressure and at Higher Temperatures (USGS Bulletin 1452).

Ryerson F. J. and McKeegan K. D. (1994) Determination of oxygen self-diffusion in åkermanite, anorthite, diopside, and spinel: Implications for oxygen isotopic anomalies and the thermal histories of Ca-Al-rich inclusions. *Geochim. Cosmochim. Acta* **58,** 3713–3734.

Sheng Y. J., Wasserburg G. J., and Hutcheon I. D. (1992) Self-diffusion of Mg in spinel and in equilibrium melts: Constraints on flash heating of silicates. *Geochim. Cosmochim. Acta* **56,** 2535–2546.

Simon S. B., Davis A. M., and Grossman L. (1999) Origin of compact type A refractory inclusions from CV3 carbonaceous chondrites. *Geochim. Cosmochim. Acta* **63,** 1233–1248.

Stolper E. (1982) Crystallization sequences of Ca-Al-rich inclusions from Allende: An experimental study. *Geochim. Cosmochim. Acta* **46,** 2159–2180.

Stolper E. and Paque J. M. (1986) Crystallization sequences of Ca-Al-rich inclusions from Allende: The effects of cooling rate and maximum temperature. *Geochim. Cosmochim. Acta* **50,** 1785–1806.

Wang J., Davis A. M., Clayton R. N., and Hashimoto A. (1999) Evaporation of single crystal forsterite: Evaporation kinetics, magnesium isotope fractionation, and implications of mass-dependent isotopic fractionation of a diffusion-controlled reservoir. *Geochim. Cosmochim. Acta* **63,** 953–966.

Yurimoto H., Morioka M., and Nagasawa H. (1989) Diffusion in single crystals of melilite: I. Oxygen. *Geochim. Cosmochim. Acta* **53,** 2387–2394.